Energy Conversion and Management 260 (2022) 115630

Contents lists available at ScienceDirect

Energy Conversion and Management

journal homepage: www.elsevier.com/locate/enconman

Modified Stirling cycle thermodynamic model IPD-MSM and its application

Chenhao Yang [a], Nailiang Zhuang [a,b,*], Weian Du [c], Hangbin Zhao [b,d], Xiaobin Tang [a,b]

[a] Department of Nuclear Science and Technology, Nanjing University of Aeronautics and Astronautics, Nanjing 211106, China
[b] Key Laboratory of Nuclear Technology Application and Radiation Protection in Astronautics, Ministry of Industry and Information Technology, Nanjing 211106, China
[c] China Ship Development and Design Center, Wuhan 430064, China
[d] College of Astronautics, Nanjing University of Aeronautics and Astronautics, Nanjing 211106, China

ARTICLE INFO

Keywords:
Stirling Cycle
Thermodynamic Model
Adiabatic Model
Helium-Xenon Mixture

ABSTRACT

A Stirling cycle is a thermoelectric conversion method with high efficiency and reliability. The Stirling cycle applies to small- and medium-sized power space nuclear reactors or radioisotope heat sources. A high-precision and well-predicted Stirling cycle thermodynamic model is the key to optimizing and improving the Stirling engine for space. The present study modified the classical Simple model by incorporating the local pressure loss into the pressure loss. An improved second-order adiabatic model based on the Simple model, namely the Incorporated Pressure Drop-modified Simple Model (IPD-MSM), was proposed. The prediction of the IPD-MSM shows well with the changing tendency of the GPU-3 Stirling engine experimental data. Moreover, this model has better prediction accuracy at high-pressure and high-frequency conditions than other adiabatic models, such as CAFS and ISAM. The thermodynamic properties of He, H_2, and Helium-Xenon mixtures in the Stirling cycle were also analyzed. Results show that the He-Xe mixture reaches the highest output power and thermal efficiency when the mole percentage of Xe is approximately 2%. The mechanism is as follows: the addition of Xe leading to the reduction in non-ideal heat transfer loss exceeds the increase in pressure loss. The addition of Xe leads the pressure loss to increase abruptly as the mole percentage of Xe exceeds 2%. The characteristics and application analysis of H_2, He, and He-Xe mixture were discussed. The present study provided theoretical support for the Stirling cycle analysis for space missions and the selection of working fluids.

1. Introduction

Space nuclear energy has been recognized as disruptive innovation and a promising substitution for conventional space energy, such as space solar panels, batteries, fuel cells, or chemical energy. Space nuclear power generally includes space nuclear reactors (SNRs) and radioisotope thermoelectric generators (RTGs). Compared with conventional space energy, space nuclear power features the absence of orientation requirements to the sun, high energy density, longevity, and a large power range (from watt to megawatt electricity) [1,2]. Since the very first SNR (SNAP-10A, Systems for Nuclear Auxiliary Power) was launched into space in 1965, 35 SNR-based satellites [3] have been successfully launched. RTGs have been the main power source for US space work since 1961. A total of 52 satellites and probes [4–6] have been utilizing RTGs as the power supply. These RTGs were launched by China, the United States, and the former Soviet Union/Russia. Thus far, all the SNRs and RTGs utilize static thermoelectric energy conversions, such as thermocouples and thermionic thermoelectric conversion. However, the efficiency of these static thermoelectric conversions does not exceed 10% [4]. Therefore, high-efficiency thermoelectric energy conversion is a vital factor and maybe the most important for large and super-large level space activities, and considerable attention should be provided to space thermoelectric conversion.

Among these dynamic thermoelectric energy conversions, a Stirling cycle is a simple and efficient method, demonstrating high efficiency (20%–40%, theoretically), compact structure, and modular organization. These features contribute to its suitability for small- and medium-level (less than 100 kW) SNRs [7] and RTGs [8]. Considering engineering application, the Stirling cycle was designed to be applied in previous SNR projects (Heat pipe-Operated Mars Exploration Reactor [9] and Fission Surface Power [10]), ongoing projects (KILOPOWER [1,11]), and RTG projects, such as Advanced Stirling RTG (NASA project) [12]. Describing and predicting the Stirling cycle and its performance is the most fundamental process. The Stirling cycle thermodynamic model is widely applied to describe and predict the process and thermal performance of the Stirling cycle. The Stirling cycle thermodynamic models can be classified as first-order, second-order,

* Corresponding author at: Department of Nuclear Science and Technology, Nanjing University of Aeronautics and Astronautics, Nanjing 211106, China.
E-mail address: zhuangnailiang@nuaa.edu.cn (N. Zhuang).

https://doi.org/10.1016/j.enconman.2022.115630
Received 7 March 2022; Received in revised form 9 April 2022; Accepted 12 April 2022

Nomenclature

General

A	Area (m^2)
c_p	Specific heat at constant pressure (J/(kg·K))
D	Diameter (m)
f_{Re}	Reynolds friction factor
L	Length (m)
$\dot{m}$	Mass flow rate (kg/s^2)
P	Pressure (loss) (Pa)
Q	Heat (loss) (W)
Re	Reynolds number
T	Temperature (K)
u	Velocity (m/s)
V	Volume (m^3)
W	Power (loss) (W)

Greek

ΔP	Pressure Loss (Pa)
ζ	Local loss coefficient
μ	Dynamic viscosity (Pa·s)
ρ	Density (kg/m^3)

Subscript

leak	Leakage
m	Mean
Shell	Regenerator shell

third-order, and fourth-order models [13]. The second-order model has been widely applied and developed due to its features of controllable error and high calculation efficiency [14].

The ideal Stirling cycle comprises two isothermal processes and two constant volume processes. However, actual processes deviate from isothermal processes, resulting in isothermal second-order models being inaccurate. Urieli and Berchowitz [15] proposed the classical Simple model. In the Simple model, the free-piston Stirling engine is divided into five working areas [15], namely compression space, k(c)cooler, regenerator, heater, and expansion space, as shown in Fig. 1. The Simple model assumes that compression and expansion are in the adiabatic processes to modify the isothermal assumptions. Moreover, non-ideal heat transfer loss in the regenerator and the pressure loss in the heat exchangers were applied as further modifications.

Numerous modifications and updates have been applied since the introduction of the Simple model, as shown in Fig. 2. Timoumi [16] proposed that losses in Stirling engines can be classified as heat loss and power loss, such as shuttle heat loss, flow resistance loss, and hysteresis loss. Sayyaadi [17,18] integrated finite speed loss, leakage loss, and other loss concepts and established CAFS and Simple-II with excellent performances. Ni et al. [19] considered the loss of the gas spring hysteresis in their Improved Simple Analytical Model (ISAM). The ISAM could effectively predict the performance of He and H_2 working fluids. Udeh et al. [20] suggested introducing the leakage between the compression and expansion room to the leakage loss modifications.

Other researchers studied the Stirling systems and expanded modeling conceptions. Cheng [21] established a non-ideal adiabatic model based on the experimental data of a 300 W Stirling engine. This model can also predict the engine torque. Araoz [22] considered combined heat and power systems, which would introduce complex effects.

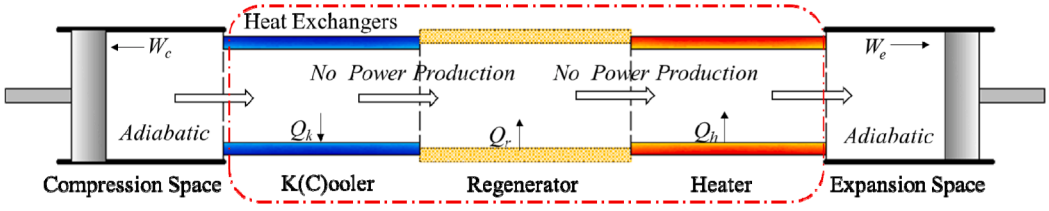

Fig. 1. The working cycle of Stirling engine based on the Simple model *Kooler* represents *Cooler* to distinguish the subscript *c*.

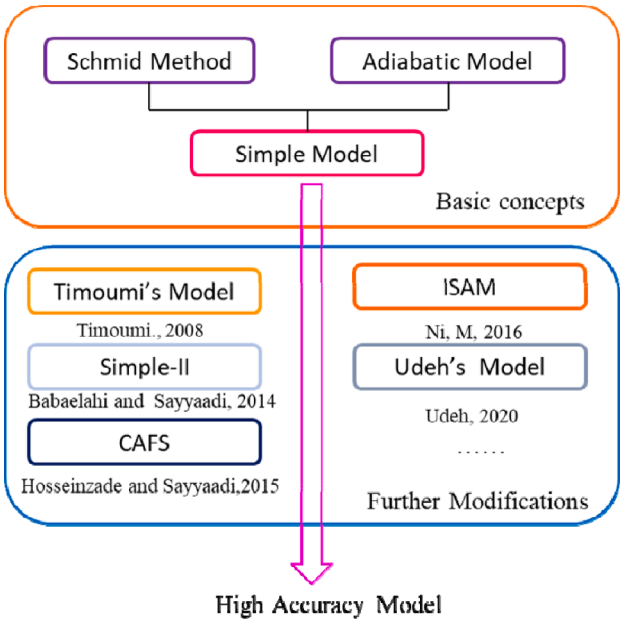

Fig. 2. Modifications and updates based on the Simple concepts.

Araoz [22] integrated the interaction between machinery and heat to improve the thermodynamic model. Saleh [23] established a comprehensive mechatronics model by integrating kinematics, dynamics, thermodynamics, heat transfer, and electrical analysis methods. Sayyaadi also proposed polytropic analysis of the Stirling engine with various losses (PSVL) [24] and polytropic finite speed thermodynamics (PFST) [25], which are polytropic models with high accuracy, based on the reference adiabatic model and modifications. However, different engines and conditions introduce numerous and unpredictable polytropic indexes. This dilemma is the crucial problem of polytropic models.

The modifications of some non-ideal losses in the Stirling cycle determine the prediction accuracy of the adiabatic model. These modifications are derived from irreversible factors in the actual Stirling cycle. Physical processes, such as heat transfer, fluid flow, and mechanical motions, are involved in the modifications. However, the predicted values at high frequencies were often substantially larger than the experimental data in the existing adiabatic models [17–20]. Moreover, the predicted trend with the operating frequency is different from the experimental values [26]. Existing modifications are still insufficient to describe the irreversible processes of the Stirling cycle. Therefore, further modifications to the loss mechanism of thermodynamic models are necessary.

A modification model (Incorporated Pressure drop-modified Simple

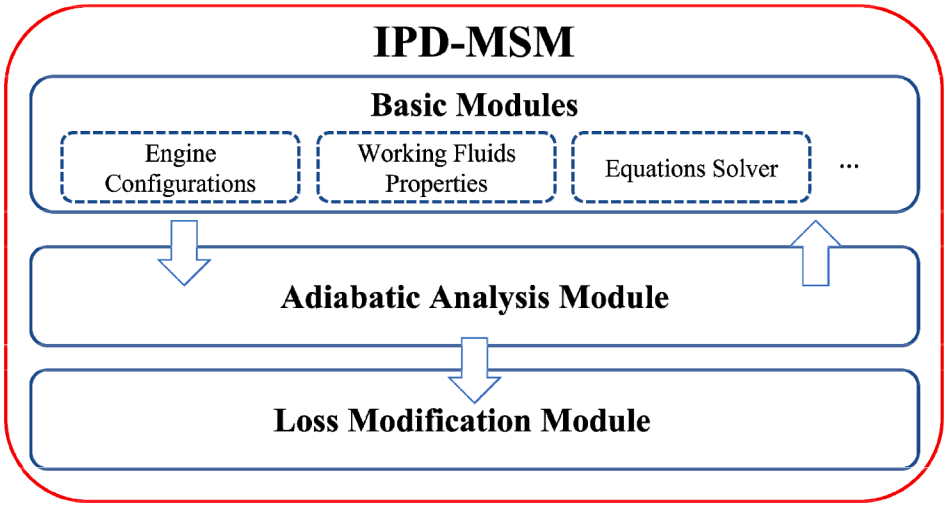

Fig. 3. The structure of the IPD-MSM.

Table 1
Modifications and correlations in IPD-MSM.

Loss items	Correlations	Descriptions
Finite speed and mechanical friction loss	$W_{FS-MF} = \int P_m(\pm\frac{aw}{c} \pm \frac{f\Delta P_{mf}}{P_m})dV$	Caused by uneven pressure distribution near the piston and mechanical friction
Leakage loss	$W_{leak} = \dot{m}_{leak} c_p T_{leak}$	Caused by fluid leakage from compression room to crankcase
Non-ideal heat exchange loss	$Q_{rloss} = Q_{r,idea}(1-\varepsilon)$	Caused by non-ideal heat transfer processes in the regenerator
Heat conduction loss	$Q_c = \lambda \frac{\Delta T}{L_{shell}} A_{shell}$	Caused by heat conduction between the heater and the cooler

Model, IPD-MSM) was proposed in the present study, incorporating the local loss and friction flow loss as the total pressure loss in the Stirling cycle. The validation of the IPD-MSM was conducted by comparison with the experimental data and other models. The thermal properties of H_2, He, and He-Xe working fluids were then discussed and analyzed using the IPD-MSM. The leakage of the He-Xe mixture was also discussed. The present study theoretically improves the prediction of free-piston Stirling engines. Additional analysis and discussions on the effects of space nuclear reactors and space environment on the Stirling cycle will be conducted soon.

2. Methodology and validation

2.1. Modification method

The IPD-MSM is composed of an adiabatic analysis module, a loss modification module, and several basic modules, as shown in Fig. 3. Among them, the loss modification module has a significant influence on the model accuracy. Modifications of heat conduction loss, non-ideal heat transfer loss, finite speed loss, and leakage loss are considered in the present study based on Simple-II [18], ISAM [19], and other model methods [20,27], as shown in Table 1. The specific derivation processes and symbol meanings can be found in the appendix and relevant works [15,18].

Pressure loss, which includes friction loss and local loss, accounts for the most extensive proportion [17–19]. The former represents loss due to friction caused by fluid viscosity, while the latter is caused by the sudden contraction/expansion of the flow cross-section or changing flow direction (bend). In the abovementioned models, including the original Simple model, pressure loss was calculated as friction loss, ignoring the local loss [26,28]. However, elbows or sudden contraction/expansion pipes are frequently found in most Stirling parts [29]. Local loss caused by these structures might not be ignored. Therefore, considering local loss and revising pressure loss may improve model accuracy.

Hence, the pressure loss in the present study adopted the local loss. The pressure loss in the present study was classified as friction loss and local loss. The correlations of the two losses are as follows.

(1) Friction loss. The pressure loss is due to the friction caused by fluid viscosity. This loss occurs during the entire process of the working fluid flow. The pressure loss can be calculated as [15]:

$$\Delta P_f = -\frac{2f_{Re}\mu u V}{d^2 A} \tag{1}$$

where μ is the dynamic viscosity, u is the fluid flow rate, V is the volume of the working area, d is the hydraulic diameter, and A is the flow cross-section area. f_{Re} is the Reynolds friction factor. It can be determined as [15]:

$$f_{Re} = \begin{cases} 16 & Re < 2000 \\ 7.343 \times 10^{-4} Re^{1.3142} & 2000 < Re < 4000 \\ 0.0791 Re^{0.75} & Re > 4000 \end{cases} \tag{2}$$

(2) Local loss. The local loss is caused by the sudden area change in flow cross-sections and can be expressed as:

$$\Delta P_j = \rho\zeta\frac{u^2}{2} \tag{3}$$

Where ρ is the density of the working fluid, and ζ is the local loss coefficient, which could be determined by the following relationship:

$$\zeta = \begin{cases} (1-\frac{A_1}{A_2})^2 & \text{sudden expansion} \\ \frac{1}{2}\left(1-\frac{A_2}{A_1}\right) & \text{sudden contraction} \end{cases} \tag{4}$$

where A_1 and A_2 respectively represent the cross-section areas of the upstream and downstream of the flow.

Work loss caused by pressure loss is:

$$W_{pl} = \oint(\Delta P_f + \Delta P_j)dV \tag{5}$$

With the pressure loss and other losses in Table 1, the loss modification module of the IPD-MSM was established.

The analysis processes of the IPD-MSM are summarized as a flow

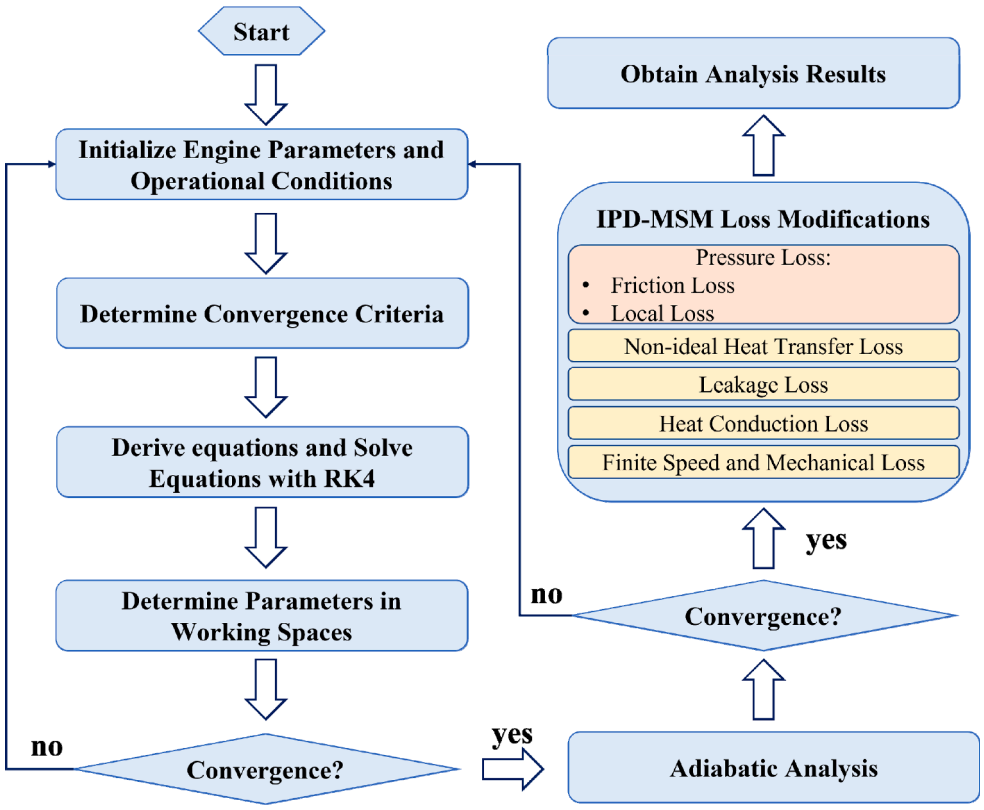

Fig. 4. Analysis flow chart of the IPD-MSM.

chart, as shown in Fig. 4. First, input data was loaded to initialize parameters and operating conditions. Then, before the adiabatic analysis and modification, the IPD-MSM would check whether parameters or initial results meet the convergence criteria. Finally, results of the IPD-MSM simulations were obtained after the adiabatic analysis and modifications. Verification and applications based on the IPD-MSM were then conducted in the following sections.

2.2. Verification of IPD-MSM

Two simulation conditions (P_m = 2.76 MPa and P_m = 4.14 MPa, He, heater temperature: 922 K, cooler temperature: 286 K) were conducted in this study to verify the IPD-MSM. Experimental data are obtained from NASA's experiments on the GPU-3 Stirling engine.

Output power and thermal efficiency are the most crucial parameters in the Stirling analysis. Therefore, output power and thermal efficiency were compared among models and the experimental data. The output work can be expressed as:

$$W_{actual} = W_{ideal} - W_{pl} - W_{leak} - W_{FS-MS} \tag{6}$$

Where W_{ideal} is:

$$W_{ideal} = W_e + W_c = \oint pdV_e + \oint pdV_c \tag{7}$$

W_e and W_c are power produced in expansion and compression space. V_e and V_c are volumes of expansion and compression space.

Then the actual thermal efficiency can be calculated as:

$$\eta_{actual} = \frac{W_{actual}}{Q_{h,act}} \times 100\% \tag{8}$$

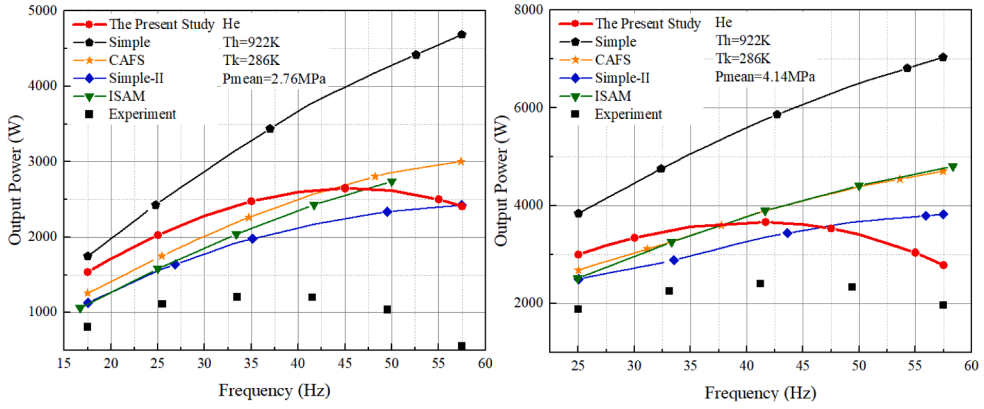

(a) P_m = 2.76 MPa (b) P_m = 4.14 MPa

Fig. 5. Comparison of output power by different models.

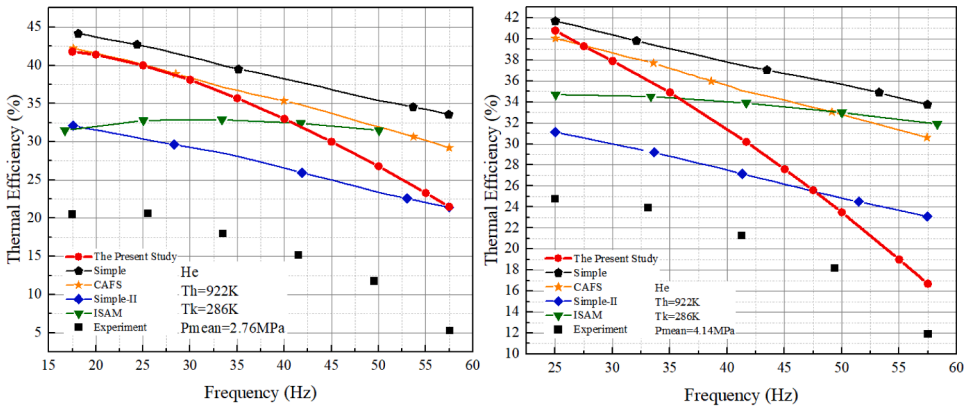

(a) P_m = 2.76 MPa (b) P_m = 4.14 MPa

Fig. 6. Comparison of thermal efficiency by different models.

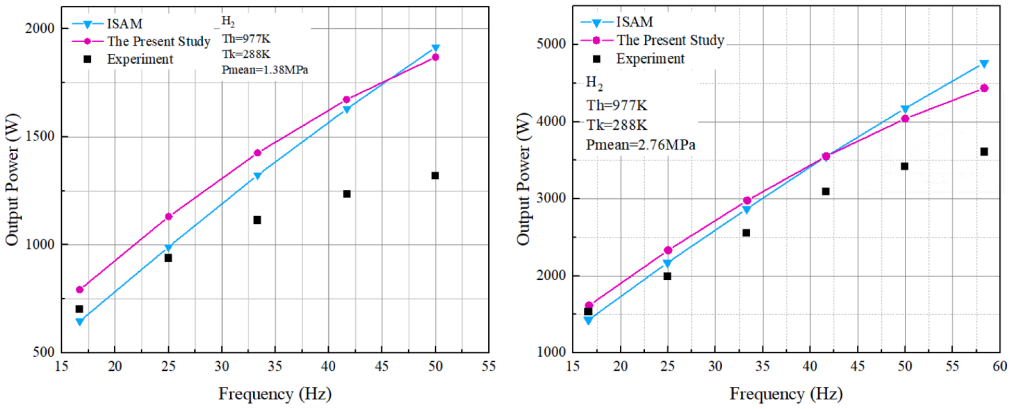

(a) P_m = 1.38 MPa (b) P_m = 2.76 MPa

Fig. 7. Impacts of frequencies on output power in the H_2 Stirling cycle.

Where $Q_{h,act}$ is the actual heat input:

$$Q_{h,act} = Q_{h,ideal} + Q_{r,loss} + Q_c \quad (9)$$

Simulation results of the IPM-MSM were compared with the experimental data of the GPU-3 [28] and simulation results of Simple, CAFS, ISAM, and Simple-II [23], as shown in Figs. 5 and 6. Rather than the exact data, this study only focused on the trend of the simulation results due to the lack of some parameters [28], such as the stroke of the power piston and the outside diameter of regenerator pipes.

Figure 5 illustrates the output power by different models and experiments. The output work by IPD-MSM primarily increases and then decreases with the increment of frequency. The changing trend of IPD-MSM is in good agreement with experimental data, while other models only show a monotonically increase. Thermal efficiency comparisons are shown in Fig. 6. The present study demonstrates a decreasing trend, which is in agreement with experimental data. The

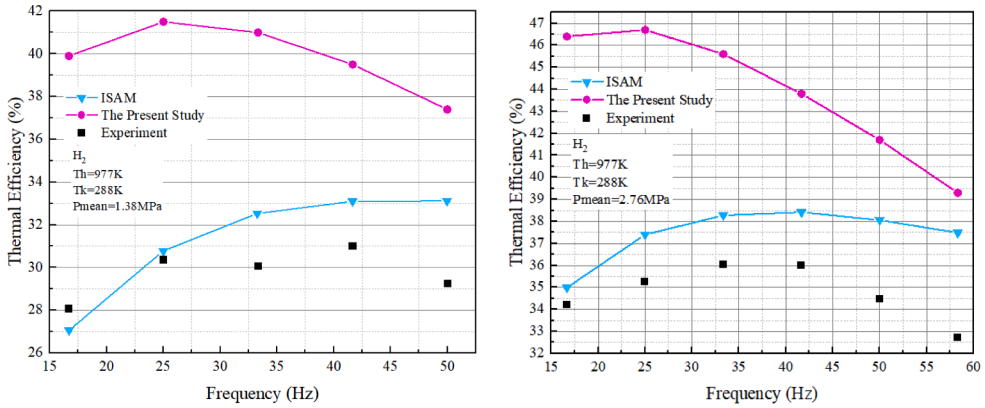

(a) P_m = 1.38 MPa (b) P_m = 2.76 MPa

Fig. 8. Impacts of frequencies on thermal efficiency in the H_2 Stirling cycle.

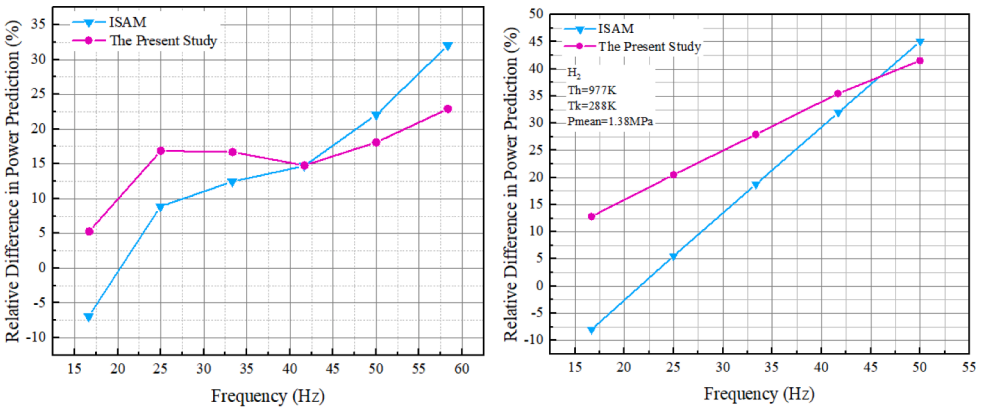

(a) P_m = 1.38 MPa (b) P_m = 2.76 MPa

Fig. 9. Relative Difference in H_2 Power Predictions of IPD-MSM and ISAM.

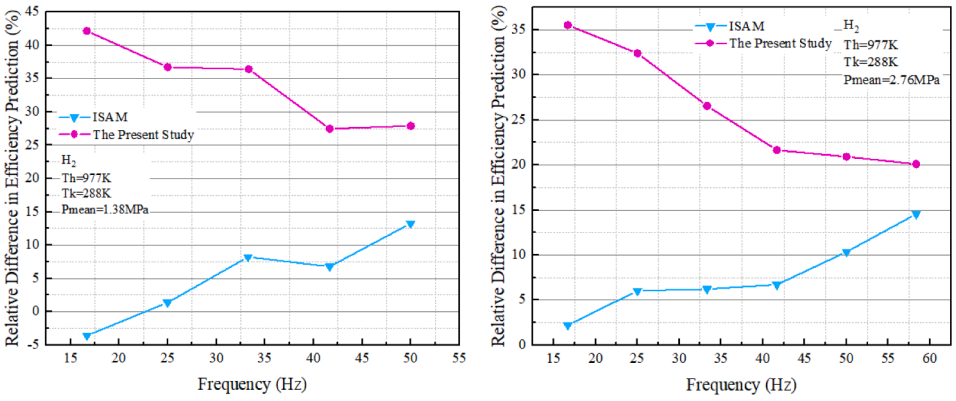

(a) P_m = 1.38 MPa (b) P_m = 2.76 MPa

Fig. 10. Relative Difference in H_2 Efficiency Predictions of IPD-MSM and ISAM.

absolute values of the slope gradually increase as the frequency increases, while other models are close to a linear decline. These results prove that the IPD-MSM could better reflect the trend of output change with frequency than other models. Moreover, the prediction values of the IPD-MSM are close to the experimental data as the mean working pressure and working frequency increase. Overall, the IPD-MSM has an adequate predictive ability on Stirling engine output parameters under different conditions.

3. Results and discussions

The most widely used working fluids, namely H_2, He, and He-Xe mixture, were simulated in this section based on IPD-MSM. The effects of He-Xe mixture molar ratios on the thermal properties and leakage were discussed. The properties of H_2, He, and He-Xe mixture under different working conditions were compared, and applicable occasions of these fluids were discussed.

3.1. Thermal performances of Stirling cycle with H_2 working fluid

H_2 is a common industrial gas usually utilized in the energy field. Theoretically, H_2 has outstanding heat transfer properties and low dynamic viscosity. Herein, the Stirling cycle of H_2 was simulated by IPD-MSM, and the results were compared with experimental data from the GPU-3, as shown in Figs. 7 and 8.

Figure 7 illustrates the output power and thermal efficiency monotonously increase with rising frequency under the P_m = 1.38 MPa (Fig. 7(a)) and P_m = 2.76 MPa (Fig. 7(b)). The thermal efficiency of H_2 is shown in Fig. 7. The thermal efficiency fluctuates at 1.38 MPa (Fig. 8 (a)). Under 2.76 MPa (Fig. 8(b)), the thermal efficiency primarily increases and then decreases with rising frequency. In addition, the thermal efficiency is higher than 26% under the working condition of P_m = 1.38 MPa and higher than 32% under the working condition P_m = 2.76 MPa.

Relative differences among models and the experimental data are illustrated in Figs. 9 and 10. The maximum relative difference in efficiency is under 45% and continually declines with the increasing frequency. Besides, the IPD-MSM has lower relative differences than the ISAM under high frequency and pressure for power prediction. Results show that IPD-MSM could be applied to simulate different working fluids.

3.2. Thermal performances of Stirling cycle with He-Xe mixtures and mole ratio

Inert gas mixtures, especially binary mixtures of He and Xe, are widely used in the Brayton cycle. El-Genk et al. [30,31] proved that adding a certain amount of Xe to He is beneficial to the heat transfer of the working fluid. However, adding Xe may also increase pressure loss. Thus, analyzing the thermal–hydraulic characteristics of the Stirling cycle with the He-Xe mixture working fluid is also important.

Among these characteristics, the physical parameters of the mixture

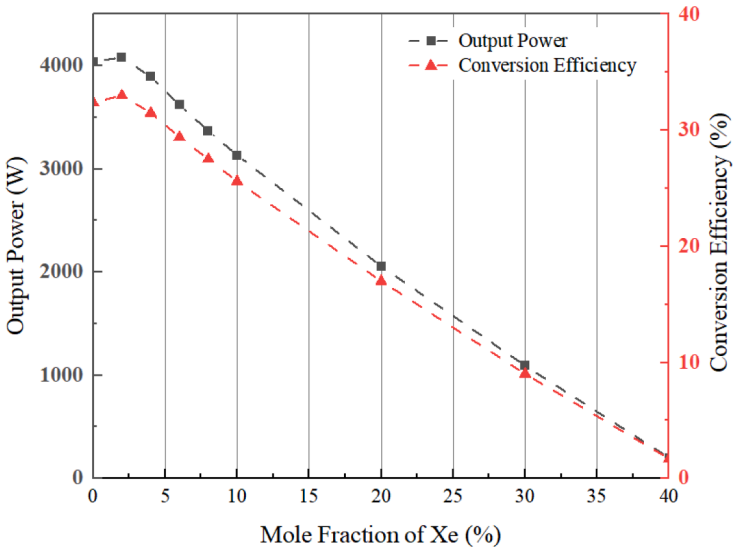

Fig. 11. Impacts of Xe fraction on output power and thermal efficiency in the He-Xe Stirling cycle.

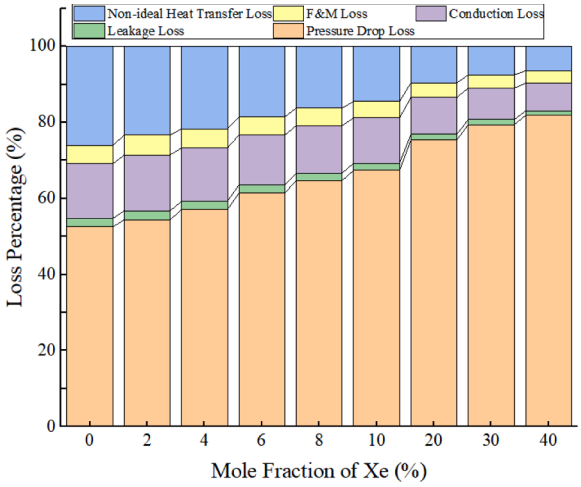

Fig. 12. Impacts of Xe fraction on loss fractions in the He-Xe Stirling cycle.

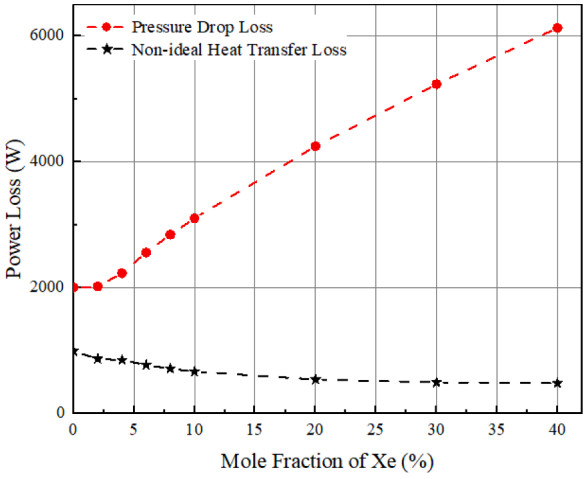

Fig. 13. Impacts of Xe fraction on power loss in the He-Xe Stirling cycle.

are the key to the simulation calculation. Tournier et al. [32] provided a calculation method based on the corresponding state principle, which can compute the thermophysical parameters of the working fluid through theoretical methods. The theoretical calculation method of Tournier et al. was combined with the REFPROP database in the present study, reducing intermediate calculations and improving calculation efficiency. The He-Xe mixture with different molar ratios as working fluid was then utilized in the IPD-MSM simulation. The output power, thermal efficiency, and various losses of the working fluids were obtained. The working parameters set for mixture analysis were $P_m = 4.14$ MPa and $f = 41.67$ Hz. The cooler and heater temperatures were 288 and 977 K, respectively.

The impacts of the Xe fraction on output power and thermal efficiency are presented in Fig. 11. The output power and cycle efficiency primarily increase as the percentage of Xe rises, reaching its maximum when the mole component of Xe is equal to approximately 2%. Afterward, the output power and thermal efficiency gradually decrease and even drop below zero when the percentage of Xe is larger than 40%. However, the He-Xe mixtures with Xe mole percentage over 40% have no value for the Stirling engine. The performance of the mixture with a Xe mole percentage above 40% was not included in the present study.

The proportion of various losses in the Stirling cycle under different molar ratios of the He-Xe mixtures was calculated as shown in Fig. 12. Among these proportions, pressure loss is the dominant part. The proportion of pressure loss gradually increases as the mole fraction of Xe rises, while proportions of conduction loss and non-ideal heat transfer loss decrease. This trend is due to the sharp increase in dynamic viscosity of the mixture after the addition of Xe, which leads to a sharp expansion in pressure loss. The density of the mixture continues to increase despite the reduction in dynamic viscosity when the molar ratio of Xe reaches 20%. Consequently, the Reynolds number ($\mathbf{Re = \rho ud/\mu}$) of the fluid continues to increase, resulting in rising pressure loss. The proportions of finite speed loss, friction loss, and leakage loss have not substantially changed in comparison.

As mentioned above, the He-Xe mixture intensifies heat transfer compared with the He. The non-ideal heat transfer loss represents the loss caused by the limited heat transfer capacity of the regenerator. This loss represents the heat transfer capacity of different He-Xe mixtures. The change in pressure loss and non-ideal heat transfer with 0–40% Xe molar ratios is shown in Fig. 13. The non-ideal heat transfer loss of the He is the largest, reaching 1000 W. The addition of the Xe significantly reduces the heat exchange loss of the working fluid. The heat loss value tends to stabilize because the mole percentage of Xe is larger than 30%. The above phenomenon shows an improvement in the heat transfer capacity of the working fluid after the addition of Xe.

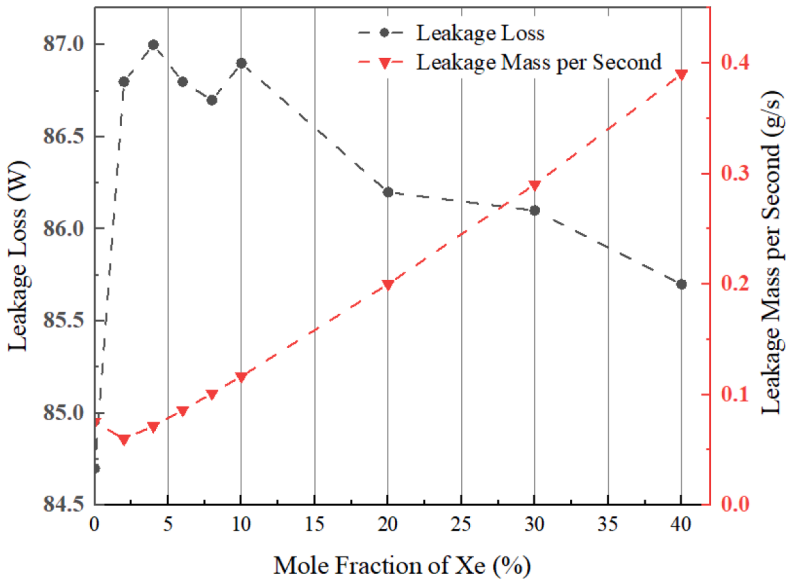

Fig. 14. Impacts of Xe fraction on leakage in the He-Xe Stirling cycle.

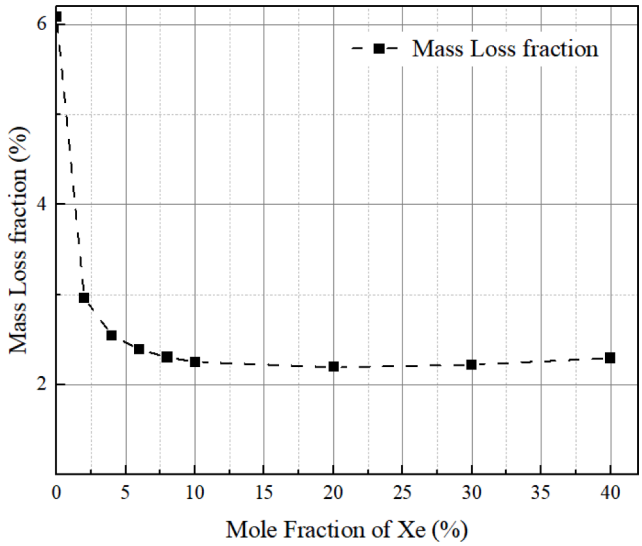

Fig. 15. Impacts of Xe fraction on mass loss friction in the He-Xe Stirling cycle.

The addition of Xe resulted in a reduction in the non-ideal heat transfer loss and increased pressure loss. The heat transfer capacity is significantly enhanced when Xe is just added. The increase in pressure loss of the mixture (17.3 W) is smaller than the decrease in non-ideal heat transfer loss (124.2 W) when the mole percentage of the Xe is 0–2%. Other loss values are relatively small in this range. This phenomenon leads to an overall output power increase. However, the increasing pressure loss would neutralize the heat transfer enhancement under the increasing percentage of the Xe. The decrease in non-ideal heat transfer loss becomes smaller than the increase in pressure loss when the Xe percentage is over 2%. Consequently, the output work and thermal efficiency of the mixture are lower than that of the He. The above reasons explain the maximum point appearance of output power and thermal efficiency.

3.3. Leakage of He-Xe mixtures

The leakage problem is crucial for space due to the space vacuum environment and the difficulties in immediately replenishing the working fluid. Relevant studies indicated that the leaked fluid is related to the molecular weight of the working fluid [33]. The IPD-MSM was used to analyze the leakage of the He-Xe mixture in this section.

The impacts of the Xe fraction on leakage by the IPD-MSM are shown in Fig. 14. Leakage loss in the present study refers to the working fluid that escapes into the crankcase along the gap between the piston and the cylinder wall. The mass loss of the working fluids was also investigated in Fig. 14, which can be expressed as:

$$\dot{m}_{loss} = f\sum_{i=1}\dot{m}_{leak,i}t_i \tag{10}$$

Where f is frequency, and $\dot{m}_{leak,i}$ is the leakage mass flow in the specific time step t_i.

The power loss caused by leakage fluctuates as the Xe increases. However, the numerical change is relatively small (approximately 2 W). The working mass leakage per second increases slightly drops and then continues to increase as shown in Fig. 14.

The total density of the mixture significantly increases despite the rise of leakage mass after the addition of Xe. This phenomenon is attributed to the larger molecular weight of Xe than He. Therefore, the proportion of mass losses drops below 2.2% and then stabilizes with the addition of Xe, as shown in Fig. 15.

3.4. Comparisons among H_2, He, and He-Xe mixture

The thermal properties of H_2, He, and He-Xe mixtures were discussed in Sections 2 and 3. Differences among working fluids were compared and discussed in this section. Three working pressures (P_m = 1.38, 2.76, and 4.14 MPa) were set in the present study considering the operating conditions of GPU-3. The mole percentage of Xe was selected as 2% for the mixture. The operation performances of three fluids are shown in Figs. 16 and 17.

Figure 16 illustrates output power comparisons among the three working fluids. The output power of H_2 is substantially higher than that of the He and He-Xe mixture. Moreover, the output power of H_2 monotonically increases with the rising frequency. This trend is due to the small dynamic viscosity and effective heat transfer characteristics of H_2. Therefore, the pressure loss and non-ideal heat transfer losses of H_2 are significantly smaller than those of the two other working fluids. Comparisons between the He and He-Xe mixture are complicated. The output power of the two fluids primarily increases and then reduces with the rising frequency. The output power of He is higher than that of the

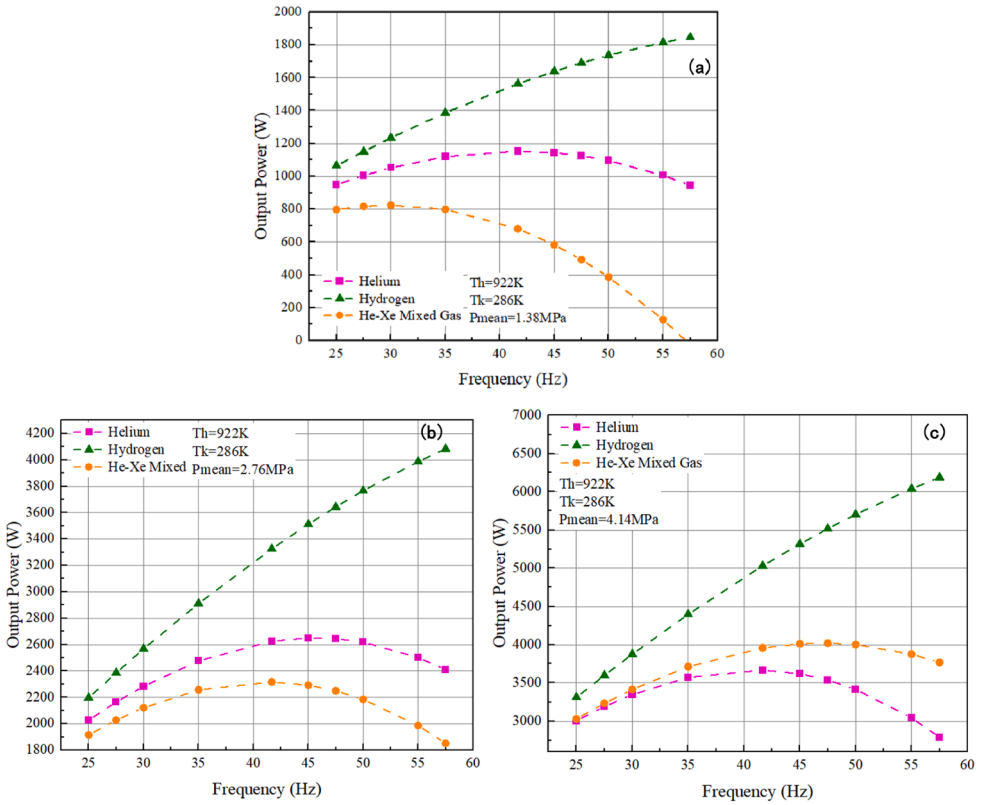

(a) $P_m = 1.38$ MPa (b) $P_m = 2.76$ MPa (c) $P_m = 4.14$ MPa

Fig. 16. Impacts of frequencies on output power in different Stirling cycles.

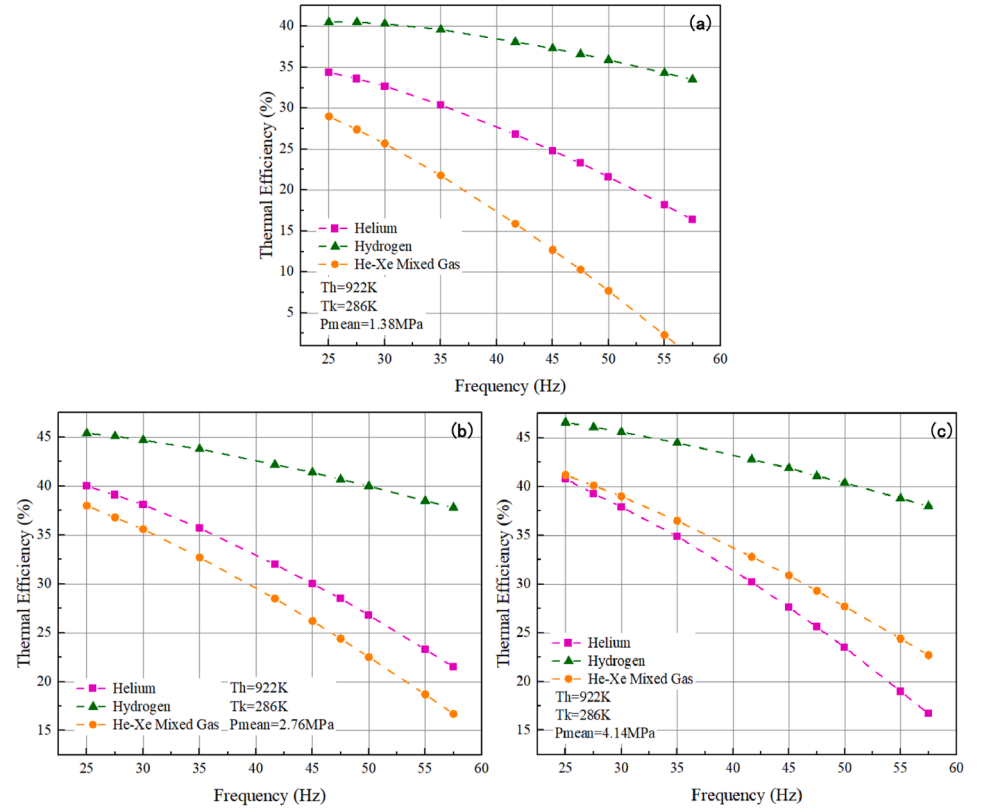

(a) $P_m = 1.38$ MPa (b) $P_m = 2.76$ MPa (c) $P_m = 4.14$ MPa

Fig. 17. Impacts of frequencies on thermal efficiency in different Stirling cycles.

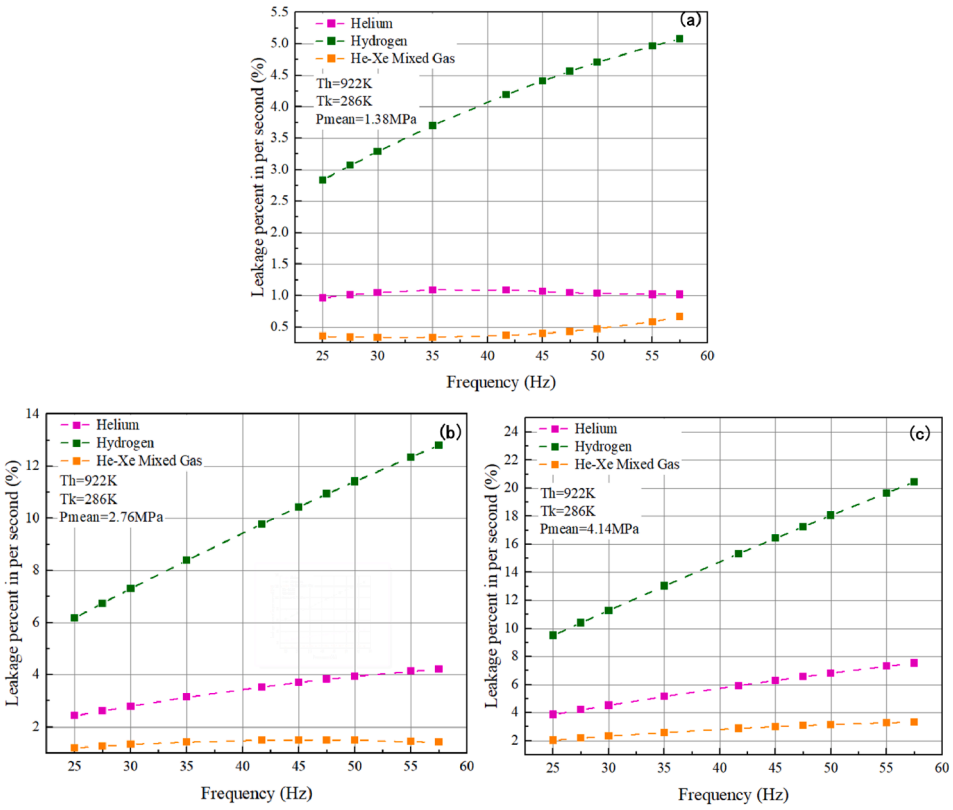

(a) P_m = 1.38 MPa (b) P_m = 2.76 MPa (c) P_m = 4.14 MPa

Fig. 18. Impacts of frequencies on mass leakage percentage in different Stirling cycles.

He-Xe under 1.38 and 2.76 MPa (Fig. 16(a), (b)). The output power of the He-Xe would even drop to zero when the mean pressure was set as 1.38 MPa. The output power of the mixture is higher than that of He under 4.14 MPa (Fig. 16(a), (c)). The dynamic viscosity of a fluid is generally slightly affected by the pressure, and the output work is the integral of the pressure to the volume. Therefore, the pressure loss of the working fluid does not change dramatically under different pressures. Meanwhile, a high average working pressure produces a high output power. Lower pressure loss is essential for producing more output power when He and He-Xe mixture output powers are small. Pressure loss differences become slightly vital when the output power of the mixture is considerably higher than that of He at high pressures.

Figure 17 shows that the thermal efficiency of the three working fluids decreases with the increasing operating frequency. The thermal efficiency of the H_2 is the highest among the three working fluids. The thermal efficiency of the He is higher than that of the He-Xe under P_m = 1.38 MPa (Fig. 13(a)) and 2.76 MPa cases (Fig. 17(b)). Meanwhile, the thermal efficiency of the He-Xe mixture is higher than that of He under P_m = 4.14 MPa (Fig. 17(c)). This finding is due to the small heat input difference between He and the He-Xe mixture. Therefore, the working fluid with a high output power can reach high thermal efficiency.

The leakage of the three working fluids is analyzed and discussed in Fig. 18. The leakage percentage generally increases with the rising mean pressure. The leakage percentage of H_2 is significantly higher than that of the two other working fluids. The leakage of the H_2 increases fast with the rising frequency. By contrast, the leakage percentage of the He-Xe mixture is the smallest among the three fluids. The mixture leakage remains at a low level as the frequency increases. The leakage percentage of the He is between H_2 and the He-Xe mixture.

The theoretical properties of H_2 are the best among the three working fluids. However, H_2 also introduces the most severe leakage problem. This defect would undoubtedly decrease the life of the space nuclear power sources in the vacuum environment. In addition, the H_2 has a risk of explosion, which limits the application. He has better properties under P_m = 1.38 and 2.76 MPa. Therefore, He is appropriate when choosing a low working pressure. By contrast, the He-Xe mixture at high pressure has superior properties. The lowest leakage percentage can also increase the working life of space nuclear power sources.

4. Conclusions

Irreversible losses in Stirling cycles were studied and modified based on the Simple model. The new thermodynamic model, IPD-MSM, was also established. Furthermore, the validation of this new model was verified by the data of the GPU-3 Stirling engine experiments and the simulations of other models. Thermal properties and leakage analysis of H_2, He, and the He-Xe mixture in the Stirling cycle were conducted. The following conclusions are presented.

(1) The Simple model was modified by incorporating the local pressure loss into the pressure loss. A new model called IPD-MSM with superior prediction trends and adequate accuracy was established.

(2) Stirling cycles with H_2, He, and He-Xe mixture as working fluids were simulated by IPD-MSM. The output power, thermal efficiency, loss values, and leakage mass of working fluids were also calculated. The optimal mixing ratio of the He-Xe mixture, which has output power and thermal efficiency higher than He and other He-Xe mixtures, was determined based on the aforementioned results.

(3) H_2 theoretically has the highest output power and thermal efficiency but would cause severe leakage and explosion problems. The output power and efficiency of He are higher than that of the He-Xe mixture under low working pressure, while the performances of the He-Xe mixture are superior under high working pressure. The optimal mixing ratio is 2% by the mole ratio of Xe under the working conditions considered in the present study.

Table A1
Modifications and correlations in IPD-MSM.

Loss items	Correlations	Descriptions
Finite speed and mechanical friction loss	$W_{FS-MF} = \int P_m(\pm\frac{aw}{c}\pm\frac{f\Delta P_{mf}}{P_m})dV$	Caused by uneven pressure distribution near the piston and mechanical friction
Leakage loss	$W_{leak} = \dot{m}_{leak}c_pT_{leak}$	Caused by fluid leakage from compression room to crankcase
Non-ideal heat exchange loss	$Q_{rloss} = Q_{r,idea}(1-\varepsilon)$	Caused by non-ideal heat transfer processes in the regenerator
Heat conduction loss	$Q_c = \lambda\frac{\Delta T}{L_{shell}}A_{shell}$	Caused by heat conduction between the heater and the cooler

CRediT authorship contribution statement

Chenhao Yang: Formal analysis, Investigation, Writing – original draft, Writing – review & editing. **Nailiang Zhuang:** Methodology, Project administration, Supervision. **Weian Du:** Visualization. **Hangbin Zhao:** Software and programming Validation. **Xiaobin Tang:** Resources, Supervision.

Declaration of Competing Interest

The authors declare that they have no known competing financial interests or personal relationships that could have appeared to influence the work reported in this paper.

Acknowledgment

This work was supported by the National Natural Science Foundation of China (Grant No. 12105142) and the Postgraduate Research & Practice Innovation Program of Jiangsu Province (Grant No. 2021K387C).

Appendix

The modification correlations in the IPD-MSM except the pressure loss are listed in the following Table A1. Detailed calculation processes were introduced in the following section.

1. Calculation of finite speed and mechanical loss

The finite speed loss and mechanical loss were caused by uneven pressure distribution near the piston and mechanical friction, which can be calculated as:

$$W_{FST-MF} = \int P_m(\pm\frac{aw}{c}\pm\frac{f\Delta P_{mf}}{P_m})dV \tag{A1}$$

where P_m is the mean working pressure, w is the speed of the piston, f is the frequency and ΔP_{mf} is the pressure loss caused by the mechanical friction. a and c are defined as:

$$\begin{aligned} a &= \sqrt{3\gamma} \\ c &= \sqrt{3R_gT} \end{aligned} \tag{A2}$$

γ is the heat ratio, R_g is the gas constant and T is the temperature.

Pressure loss caused by the mechanical friction ΔP_{mf} in Eq. A(1) can be expressed as:

$$\Delta P_{mf} = \frac{(0.4+0.0045w)\times 10^5}{3\mu}(1-\frac{1}{r_v}) \tag{A4}$$

where r_v is the compression ratio, and μ can be determined by:

$$\mu = 1-\frac{1}{3r_v} \tag{A5}$$

In Eq. A(1), the $\pm$ represents the compression process (+) and the expansion process (-), respectively.

2. Calculation of the leakage loss

The leakage loss is caused by fluid leakage from compression room to crankcase. The power loss caused by the working fluid leakage is:

$$W_{leak} = \dot{m}_{leak}c_pT_{leak} \tag{A6}$$

where c_p is the specific heat capacity at constant pressure, and T_{leak} is the temperature of the leakage working fluid. The leakage mass flow $\dot{m}_{leak}$ can be calculated as:

$$\dot{m}_{leak} = \pi d_{cylinder}\frac{P_c+P_{buffer}}{4R_gT_{leak}}(w_cJ-\frac{J^3}{6}\frac{P_c-P_{buffer}}{L}) \tag{A7}$$

where Pc is the pressure in compression space, $d_{cylinder}$ is the diameter of the cylinder, P_{buffer} is the pressure of buffer space, J is the gap between cylinder and piston and L is the length of the piston.

3. Calculation of the non-ideal heat transfer loss

This loss is caused by non-ideal heat transfer processes in the regenerator. The non-ideal heat transfer loss can be calculated as:

$$Q_{rloss} = Q_{r,idea}(1-\varepsilon) \tag{A8}$$

where $Q_{r,ideal}$ is the amount of regenerator heat transferred in ideal process, and ε is the effectiveness of the regenerator, which is:

$$\varepsilon = \frac{NTU}{1+NTU} \tag{A9}$$

NTU is the number of heat transfer unit. It can be determined by:

$$NTU = \frac{StA_{wg}}{A} \tag{A10}$$

where St is the Stanton number, Awg is the wet area of the working fluid in the regenerator, and A is the cross-section area of the regenerator. The St can be expressed as:

$$St = 0.023Re^{-0.2}Pr^{-0.6} \tag{A11}$$

Re and *Pr* are the Reynolds number and Prandtl number respectively.

4. Calculation of the heat conduction loss

The heat conduction loss is caused by heat conduction between the heater and the cooler. The heat conduction loss is obtained by Fourier's Law as:

$$Q_c = \lambda\frac{\Delta T}{L_{shell}}A_{shell} \tag{A12}$$

where λ is the heat conduction coefficient, ΔT is the temperature difference between the heater and cooler, L_{shell} is the length of the regenerator shell, and A_{shell} is the heat conduction area of the regenerator shell.

References

[1] Gibson MA, Oleson SR, Poston DI, McClure P. NASA's Kilopower Reactor Development and the Path to Higher Power Missions. 2017 IEEE Aerospace Conference. Big Sky, MT, USA: IEEE; 2017. p. 1-14.

[2] El-Genk MS. Deployment history and design considerations for space reactor power systems. Acta Astronaut 2009;64:833–49. https://doi.org/10.1016/j.actaastro.2008.12.016.

[3] Stanculescu A. The role of nuclear power and nuclear propulsion in the peaceful exploration of space. VIENNA: International Atomic Energy Agency; 2005.

[4] Yang J, Ke G, Su Z. Space Nuclear Power (in Chinese). Shanghai: Shanghai Jiao Tong University Press; 2016.

[5] Lorenz RD, Clarke ES. Influence of the Multi-Mission Radioisotope Thermoelectric Generator (MMRTG) on the local atmospheric environment. Planet Space Sci 2020;193:105075. https://doi.org/10.1016/j.pss.2020.105075.

[6] Ye P, Sun Z, Zhang H, Zhang L, Wu X, Li F. Mission design of Chang'e-4 probe system. Scientia Sinica (Technologica) 2019;49:124–37.

[7] Mason LS. A comparison of Brayton and Stirling space nuclear power systems for power levels from 1 kilowatt to 10 megawatts. Space Technology and Applications International Forum-STAIF 2001. Cleveland, Ohio: American Institute of Physics; 2001. p. 1017-1022.

[8] Chan J, Wood JG, Schreiber JG. Development of advanced stirling radioisotope generator for space exploration. Space Technology and Applications International Forum-STAIF 2007. Albuquerque, New Mexico, USA: American Institute of Physics; 2007. p. 615-623.

[9] Poston DI. The Heatpipe-Operated Mars Exploration Reactor (HOMER). In: AIP Space Technology and Applications International Forum. Albuquerque, New Mexico: American Institute of Physics; 2001. p. 797–804.

[10] Mason L, Poston D. A summary of NASA architecture studies utilizing fission surface power technology. Eighth International Energy Conversion Engineering Conference (IECEC). Nashville, TN; 2011. p. 6599.

[11] Gibson MA, Poston DI, McClure P, Godfroy T, Sanzi J, Briggs MH. The Kilopower reactor using Stirling TechnologY (KRUSTY) nuclear ground test results and lessons learned. 2018 International Energy Conversion Engineering Conference. Cincinnati, Ohio; 2018. p. 4973.

[12] Dugala GM. Stirling Convertor Controller Development at NASA Glenn Research Center. In: in AIAA Propulsion and Energy Forum; 2018. p. 9–11.

[13] Ahmed F, Hulin H, Khan AM. Numerical modeling and optimization of beta-type Stirling engine. Appl Therm Eng 2019;149:385–400. https://doi.org/10.1016/j.applthermaleng.2018.12.003.

[14] Ni M, Xiao G, Cen K. Analysis of Stirling Cycles and Design of Stirling Engines (in Chinese). Beijing: China Science Publishing & Media Ltd; 2019.

[15] Urieli I, Berchowitz DM. Stirling cycle engine analysis. UK: A. Hilger Bristol; 1984.

[16] Timoumi Y, Tlili I, Ben NS. Performance optimization of Stirling engines. Renewable Energy 2008;33:2134–44. https://doi.org/10.1016/j.renene.2007.12.012.

[17] Hosseinzade H, Sayyaadi H. CAFS: the combined adiabatic-finite speed thermal model for simulation and optimization of Stirling engines. Energy Convers Manage 2015;91:32–53. https://doi.org/10.1016/j.enconman.2014.11.049.

[18] Babaelahi M, Sayyaadi H. Simple-II: a new numerical thermal model for predicting thermal performance of Stirling engines. Energy 2014;69:873–90. https://doi.org/10.1016/j.energy.2014.03.084.

[19] Ni M, Shi B, Xiao G, Peng H, Sultan U, Wang S, et al. Improved simple analytical model and experimental study of a 100 W β-type Stirling engine. Appl Energy 2016;169:768–87.

[20] Udeh GT, Michailos S, Ingham D, Hughes KJ, Ma L, Pourkashanian M. A new non-ideal second order thermal model with additional loss effects for simulating beta Stirling engines. Energy Convers Manage 2020;206:112493. https://doi.org/10.1016/j.enconman.2020.112493.

[21] Cheng C, Yang H, Keong L. Theoretical and experimental study of a 300-W beta-type Stirling engine. Energy 2013;59:590–9. https://doi.org/10.1016/j.energy.2013.06.060.

[22] Araoz JA, Salomon M, Alejo L, Fransson TH. Numerical simulation for the design analysis of kinematic Stirling engines. Appl Energy 2015;159:633–50. https://doi.org/10.1016/j.apenergy.2015.09.024.

[23] Tavakolpour-Saleh AR, Zare S, Bahreman H. A novel active free piston Stirling engine: modeling, development, and experiment. Appl Energy 2017;199:400–15. https://doi.org/10.1016/j.apenergy.2017.05.059.

[24] Hosseinzade H, Sayyaadi H, Babaelahi M. A new closed-form analytical thermal model for simulating Stirling engines based on polytropic-finite speed thermodynamics. Energy Convers Manage 2015;90:395–408. https://doi.org/10.1016/j.enconman.2014.11.043.

[25] Babaelahi M, Sayyaadi H. Modified PSVL: a second order model for thermal simulation of Stirling engines based on convective–polytropic heat transfer of working spaces. Appl Therm Eng 2015;85:340–55. https://doi.org/10.1016/j.applthermaleng.2015.03.018.

[26] Ahmadi MH, Ahmadi M, Pourfayaz F. Thermal models for analysis of performance of Stirling engine: a review. Renew Sustain Energy Rev 2017;68:168–84. https://doi.org/10.1016/j.rser.2016.09.033.

[27] Dai Z, Wang C, Zhang D, Tian W, Qiu S, Su GH. Design and analysis of a free-piston stirling engine for space nuclear power reactor. Nucl Eng Technol 2021;53(2):637–46.

[28] Ahmed F, Huang H, Ahmed S, Wang X. A comprehensive review on modeling and performance optimization of Stirling engine. Int J Energy Res 2020;44:6098–127. https://doi.org/10.1002/er.5214.

[29] Martini WR. Stirling engine design manual: US Department of Energy, Office of Conservation and Solar Applications; 1978.
[30] El-Genk MS, Tournier J. Noble gas binary mixtures for gas-cooled reactor power plants. Nucl Eng Des 2008;238:1353–72. https://doi.org/10.1016/j.nucengdes.2007.10.021.
[31] El-Genk MS, Tournier J. On the use of noble gases and binary mixtures as reactor coolants and CBC working fluids. Energy Convers Manage 2008;49:1882–91. https://doi.org/10.1016/j.enconman.2007.08.017.
[32] Tournier J, El-Genk M, Gallo B. Best estimates of binary gas mixtures properties for closed Brayton cycle space applications. 4th International Energy Conversion Engineering Conference and Exhibit (IECEC). San Diego, California; 2006. p. 4154.
[33] Yu P. Research on Quasi Steady Stirling Cycle Analysis Model and Energy Loss Mechanism: Zhejiang University; 2020.